Analysis of Field-Effect Passivation in Textured and Undiffused Silicon Surfaces

Deniz Turkay,[1,2,*] Cagil Koroglu,[3,4] and Selcuk Yerci[1,2,4,†]
[1] *Center for Solar Energy Research and Applications, Ankara 06800, Turkey*
[2] *Department of Micro and Nanotechnology, Middle East Technical University, Ankara 06800, Turkey*
[3] *Department of Electrical Engineering, Stanford University, Stanford, California 94035, USA*
[4] *Department of Electrical and Electronics Engineering, Middle East Technical University, Ankara 06800, Turkey*

(Received 5 January 2019; revised manuscript received 1 August 2019; published 13 September 2019)

In this work, we present a numerical analysis comparing the field-effect passivation provided by fixed dielectric charges on planar and textured undiffused silicon surfaces. We focus particularly on the ratio of effective surface recombination velocities (S_{eff}) of planar and textured surfaces ($\sigma = S_{\text{eff,textured}}/S_{\text{eff,planar}}$) utilizing the same fixed dielectric charge density (Q_f) under the same injection conditions. To ensure a difference between the space-charge region profiles of textured and planar surfaces, we specifically analyze structures with large aspect ratios and submicron feature sizes. A wide range of Q_f (1×10^7 to 1×10^{13} cm^{-2}) having both negative and positive polarities is covered in the analysis. We show that σ approximately follows the surface area enhancement for very small and large Q_f, which induce weak band-bending and strong accumulation or inversion conditions, respectively. For moderately large Q_f, on the other hand, σ shows a stronger deviation from the surface area enhancement. To elucidate the underlying physical mechanisms leading to the nonmonotonous relation between σ and Q_f, we analyze the electrostatics of opposing charged surfaces. We show that an enhanced field-effect passivation is not realized along a large portion of a textured surface having a large Q_f due to the significant carrier localization near the surface.

DOI: 10.1103/PhysRevApplied.12.034026

I. INTRODUCTION

Front surface reflection and recombination are two prominent loss mechanisms that can limit the performance of high-efficiency silicon solar cells, particularly of those with undiffused front surfaces (e.g., interdigitated back contact cells) [1,2]. Texturing the front surface results in an improved optical performance, yet it typically comes at the cost of enhanced surface recombination losses due to the larger surface area compared to that of a planar structure. In addition, these losses are further elevated if the passivation quality at the textured surface is inferior to that of the planar surface. For instance, random upright pyramid textures, which is the industry standard for the texturization of monocrystalline silicon solar cells, provide less than 2% weighted reflectance when coated with an antireflection layer [3]. In return, the surface area is enhanced roughly 1.7 times compared to that of a planar surface. It was shown that the ratio of effective surface recombination velocities (S_{eff}) of textured and planar surfaces ($\sigma = S_{\text{eff,textured}}/S_{\text{eff,planar}}$) depends on several factors besides the surface area enhancement for these structures, such as stress-induced defects arising due to the vertices and edges in the textured structures [4,5], and the differences between the degree of passivation that can be provided to the exposed crystal planes of the textured and planar surfaces [4–7]. Overall, σ was shown to be either approximately proportional to the surface area enhancement or greater than that for undiffused random pyramid textured surfaces passivated with commonly used dielectrics such as SiO_2, SiN_x, and Al_2O_3 [4–6].

Alternative to random upright pyramids, high-aspect-ratio surface structures having very low broadband reflectance without an antireflection coating have also been demonstrated with reasonable S_{eff} [8,9] and surface saturation current densities (J_{0s}) [10] despite the significant surface area enhancement. One of the key aspects that enabled these successful demonstrations has been the use of highly conformal thin dielectric films surrounding the surface features, deposited by atomic layer deposition [8–10]. Besides the outstanding conformality, the utilized dielectric films (e.g., Al_2O_3) commonly have a high fixed dielectric charge density (Q_f) near the silicon-dielectric interface [11], leading to a significant suppression of one type of carrier concentration, and thus the recombination rate, near the surface. This passivation mechanism, based on the modification of carrier concentrations rather than

---

[*] deniz.turkay@metu.edu.tr
[†] syerci@metu.edu.tr

defect properties, is commonly referred to as field-effect passivation. Notably, σ extracted from the experimental measurements were below the surface area enhancement for the high-aspect-ratio surfaces utilizing such films [9,10,12]. The findings are generally attributed to an enhanced field-effect passivation, where the carrier concentration suppression within a small texture is regarded as more effective than that in a planar structure [9,12–14]. Yet, an explicit numerical analysis comparing the field-effect passivation in textured and planar structures has not been provided so far.

Here, we present an analysis comparing the field-effect passivation between textured and planar surfaces through two-dimensional simulations, and calculations accounting for the opposing dielectric coated facets. To imitate the experimental conditions where σ appears to be below the surface area enhancement and to ensure a modification in space charge region (SCR) profiles upon texturing, we specifically analyze structures with large aspect ratios and submicron feature sizes. Assuming defect and Q_f profiles independent of the surface geometry, and a high carrier lifetime in the bulk, we confine the analysis to changes in recombination rates that arise solely due to modifications in carrier concentrations at the surface upon texturing.

II. METHODOLOGY

In the presence of fixed dielectric charges near the dielectric-silicon interface, a compensating space charge is induced in silicon to preserve charge neutrality. The region extending from the surface into the silicon, containing a nonzero space charge density [$\rho = q(p - n + N_D - N_A)$, where p, n, N_D, and N_A are hole, electron, donor, and acceptor concentrations, respectively], is commonly called a space charge region (SCR), which is illustrated by the dark gray regions in Figs. 1(a) and 1(b) for planar and textured surfaces, respectively.

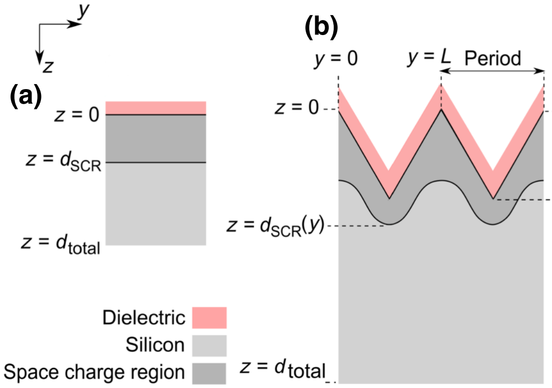

FIG. 1. Schematics of the (a) planar and (b) triangular textured structures used in the simulations, where the aspect ratio, R, is the ratio of height to period.

Here, we define the minimum depth of the SCR (d_{SCR}) in relation with the Debye-Hückel length, L_D [15], formulated as

$$L_D = \sqrt{\frac{kT\epsilon_0\epsilon_s}{q^2(n_b + p_b)}}, \tag{1}$$

where ϵ_0 is the permittivity of vacuum; ϵ_s is the relative permittivity of silicon; and n_b and p_b are the electron and hole concentrations in the quasineutral base near $z = d_{\text{SCR}}$, respectively. We assume that if the magnitude of induced electrostatic potential (ψ) is larger than a predetermined threshold [chosen as $\psi_{\text{th}} = (kT/q)/10$ in this work], the depth of the SCR (Fig. 1) increases according to

$$d_{\text{SCR}} = d(|\psi| = \psi_{\text{th}}) + L_D, \tag{2}$$

where d is the distance from the surface where $|\psi| = \psi_{\text{th}}$, and we assume that $\psi = 0$ in the quasineutral base.

Recombination processes in the SCR are commonly parametrized by S_{eff} [16,17]. The integrated recombination rate in the SCR is lumped to the boundary separating the SCR and quasineutral base, as represented with the black line at $z = d_{\text{SCR}}$ in Fig. 1, and divided by the excess minority carrier concentration, $\Delta n = \Delta p$ (assuming quasineutrality), at that boundary, resulting in the one-dimensional form

$$S_{\text{eff}} = \frac{1}{\Delta n}\left(U_s + \int_0^{d_{\text{SCR}}} U_b(z)\, dz\right), \tag{3}$$

where U_b is the sum of Auger, radiative, and Shockley-Read-Hall (SRH) recombination rates in the bulk part of the SCR, and U_s is the surface recombination rate modeled by the SRH formalism [18–20], assuming a trap state located at a single energy level as

$$U_s = \left(n_s p_s - n_i^2\right)\left(\frac{n_s + n_1}{S_{p0}} + \frac{p_s + p_1}{S_{n0}}\right)^{-1}, \tag{4}$$

where $n_1 = n_i \exp[(E_t - E_i)/kT]$; $p_1 = n_i \exp[(E_i - E_t)/kT]$; n_i and E_i are the intrinsic carrier concentration and energy level, respectively; E_t is the energy level of the trap state; k is the Boltzmann constant; T is the temperature; n_s and p_s are the electron and hole concentrations at the surface, respectively; and S_{n0} and S_{p0} are the surface recombination parameters for electrons and holes, respectively.

In this work, we construct the structures shown in Fig. 1 using an electrical simulation tool, Silvaco ATLAS [21], to calculate the S_{eff} of planar and textured surfaces. We utilize a two-dimensional form of Eq. (3) as

$$S_{\text{eff,2D}} = \frac{1}{L\Delta n}\left(\int_{\Omega} U_s(y,z)\, ds + \iint_{\Theta} U_b(y,z)\, dy\, dz\right), \tag{5}$$

where Ω is the path along the surface of the texture within a period length of L in the y direction [Fig. 1(a)], ds is the arc length, Θ is the cross-sectional region of the bulk of the SCR, and Δn is the excess carrier concentration that is assumed to be constant along $d_{\text{SCR}}(y)$. We place the rear surface at $z = d_{\text{total}}$ far enough not to electrically interact with the SCR at the front surface (i.e., $d_{\text{SCR}} \ll d_{\text{total}}$). Under electrical conditions resembling those in a quasi-steady-state photoconductance measurement, we apply a spatially uniform generation rate in silicon as the input and extract the Δn and the recombination rates in the SCR under steady state.

In the simulations, we employ classical physics, Fermi-Dirac carrier statistics, the unified mobility model of Klaassen [22], the band-gap narrowing model of Schenk [23], and the Auger recombination model of Richter [24]. We focus mainly on textures having aspect ratios (R = height to period) larger than that of random pyramid textures (approximately 0.7), and unless stated otherwise, these structures have a period, L, of 0.2 μm. To achieve pronounced differences between the SCR profiles in textured and planar structures, we use an n-type silicon bulk with a relatively low $N_D = 1 \times 10^{15}$ cm^{-3} and $\Delta n = 1 \times 10^{14}$ cm^{-3}. We set the SRH lifetimes of both electrons (τ_{n0}) and holes (τ_{p0}) to 30 ms, representing the carrier lifetimes in a high-quality silicon wafer. We assume that the energy level of trap states both at the bulk and the surface are located at $E_t = E_i$. In accordance with the previous work on interface properties between silicon and dielectrics, we set $S_{n0}/S_{p0} = 100$ [25–27] and $S_{n0} = 5 \times 10^3$ cm/s [28,29]. We assume that S_{n0}, S_{p0}, Q_f, τ_{n0}, and τ_{p0} are independent of surface geometry. We use the subscript s throughout the paper to denote the value of a parameter specifically at the surface. Lastly, note that the units of Q_f and ρ are, in fact, the elementary charge per unit volume and area, respectively. However, we omit the "elementary charge" in the units for simplicity, resulting in the units cm^{-2} and cm^{-3} for Q_f and ρ, respectively.

III. RESULTS AND DISCUSSION

A. Comparison of S_{eff} in textured and planar surfaces

S_{eff} of the planar surface and the textured surface with an R of 5 is illustrated with respect to negative and positive Q_f in Figs. 2(a) and 2(b), respectively. In addition, Figs. 2(c) and 2(d) show σ for three different R values of 2, 5, and 8, demonstrating the similarities in the trends of σ for textures having various aspect ratios. Depending on the deviation of σ from the surface area enhancement and the magnitude of Q_f, we identify three regions as highlighted in Figs. 2(c) and 2(d). The range of small Q_f ($< 5 \times 10^8$ cm^{-2}) with negligible deviations in σ from the surface area enhancement is denoted as region I. The range of moderate Q_f (5×10^8 to 2×10^{11} cm^{-2}) where σ deviates considerably from the surface area enhancement is denoted as region II. The range of large Q_f ($> 2 \times 10^{11}$ cm^{-2}) where σ is approximately equal to the surface area enhancement is denoted as region III.

In region I, ρ induced in silicon is relatively small and p and n in the SCR are very similar to their respective

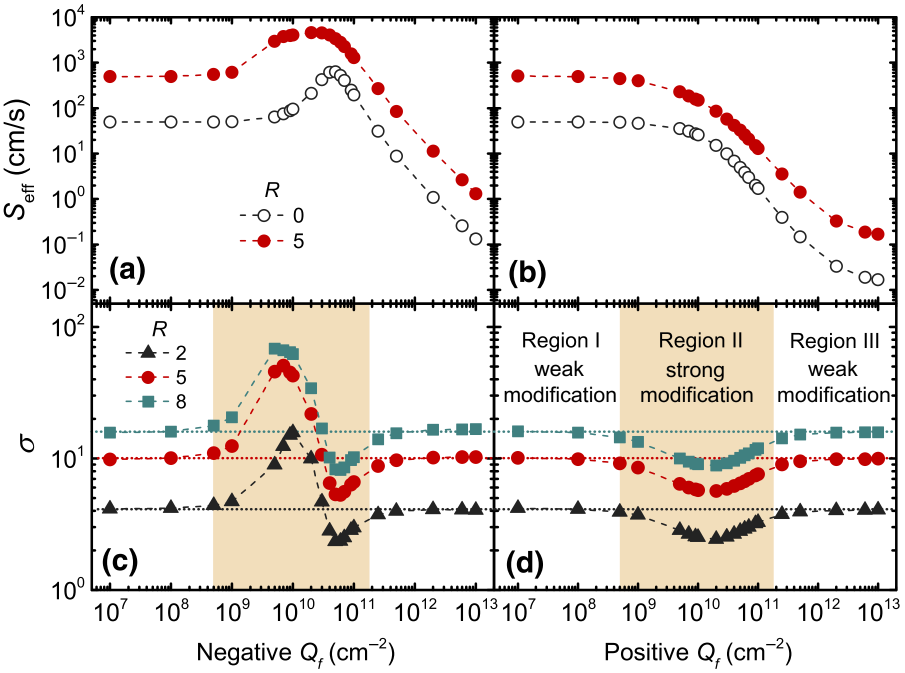

FIG. 2. S_{eff} calculated for (a) negative and (b) positive Q_f for planar and textured ($R = 5$) surfaces. σ vs Q_f for R values of 2, 5, and 8 for (c) negative and (d) positive Q_f. The lateral dotted lines in (c) and (d) represent the surface area enhancement [$= (1 + 4R^2)^{1/2}$]. The dashed lines connecting the data points are provided to guide the eye. Regions I, II, and III are defined according to the significance of carrier concentration modifications upon texturing and the magnitude of Q_f.

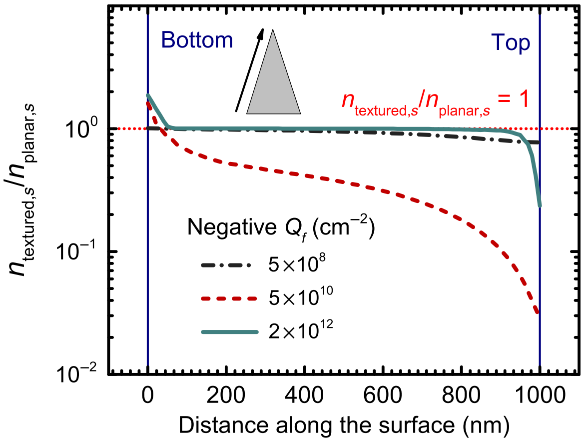

FIG. 3. The ratio of electron concentration along the texture surface (starting from the bottom of the facet to its top) to that at the planar surface with the same Q_f. The aspect ratio of the texture is 5. The gray triangle represents the geometry of the texture and is not to scale.

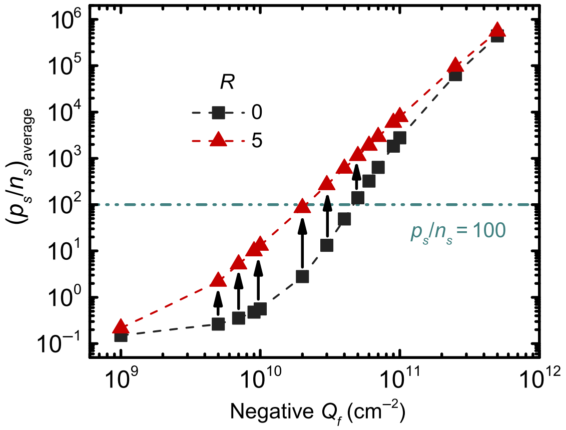

FIG. 4. The average of the p_s/n_s ratio at the surface of the planar and the textured structures with an aspect ratio of 5. Arrows indicate the change in the average p_s/n_s ratio upon texturing.

concentrations in the quasineutral base (i.e., n_b and p_b) for both negative and positive Q_f and for both planar and textured surfaces. Because of the small band bending near the surface ($|\psi| \ll kT/q$), the SCR is called to be in the weak band-bending regime [30]. As a result, S_{eff} is approximately equal to S_{p0} (= 50 cm/s) under low-injection conditions (i.e., $n \ll \Delta n$) for a planar surface [Figs. 2(a) and 2(b)]. Upon texturing in this regime, relative changes in free carrier concentrations are negligible along the surface (i.e., $n_{\mathrm{textured},s} \approx n_{\mathrm{planar},s}$ and $p_{\mathrm{textured},s} \approx p_{\mathrm{planar},s}$), and $n_{\mathrm{textured},s}/n_{\mathrm{planar},s}$ is near unity along the surface as shown in Fig. 3 for a negative Q_f of $< 5 \times 10^8$ cm^{-2} representing the upper bound of region I. Since U_s is proportional to p_s under low-injection conditions ($U_s \approx p_s S_{p0}$), the relative change in U_s along the surface is also negligible. As a result, σ follows the surface area enhancement.

In region II, the weak band-bending regime is subsequently followed by the depletion (i.e., both n_s and $p_s < N_D$); weak inversion (i.e., roughly $1 < n_s/p_s < 10$ for $\Delta n = 1 \times 10^{14}$ cm^{-3} and $N_D = 1 \times 10^{15}$ cm^{-3}); and strong inversion regimes (i.e., $10 < p_s/n_s$) for a negative Q_f. The dominant mechanism affecting S_{eff} and σ in this region is the ratio of p_s to n_s and its effect on U_s. According to the SRH formulation in Eq. (4), a maximum in U_s occurs when p_s/n_s equals to S_{n0}/S_{p0} (= 100 in this study) for a constant Δn. Therefore, S_{eff} increases with Q_f as p_s/n_s approaches S_{n0}/S_{p0} and maximizes at a Q_f of 5×10^{10} cm^{-2} for the planar surface [Fig. 2(a)]. For a larger Q_f beyond this maximum, U_s depends mainly on n_s ($U_s \approx n_s S_{n0}$), which decreases with Q_f. Upon texturing, the relative changes in free carrier concentrations along a large portion of the surface are significantly more pronounced compared to those in region I as shown in Fig. 3 for a Q_f of 5×10^{10} cm^{-2}. Moreover, because of the overall decrease in n_s and increase in p_s upon texturing, the p_s/n_s ratio is larger along the texture surface on average compared to the p_s/n_s on the planar surface with the same Q_f. In this respect, Fig. 4 shows the average p_s/n_s vs Q_f for the planar and textured structures, where the arrows indicate the changes in p_s/n_s upon texturing. Up to a negative Q_f of approximately 3×10^{10} cm^{-2}, texturing results in the average p_s/n_s ratio approaching a value near S_{n0}/S_{p0}, indicating that, on average, U_s along the surface becomes higher than that of a planar surface. As a result, σ attains values above the surface area enhancement. Conversely, a p_s/n_s ratio that is close to the S_{n0}/S_{p0} ratio in a planar structure (i.e., $Q_f = 5 \times 10^{10}$ cm^{-2}) is driven away from it upon texturing (Fig. 4). Consequently, U_s is reduced on average and σ attains values that are below the surface area enhancement [Fig. 2(c)]. When strong inversion conditions start to prevail for a Q_f greater than roughly 5×10^{10} cm^{-2}, σ still deviates from the surface area enhancement, yet it increases and approaches the area enhancement with Q_f.

For a positive Q_f in region II, weak band-bending is followed by accumulation and strong accumulation (i.e., $10 \ll n_s/p_s$) regimes. Since S_{n0} is greater than S_{p0}, and n_s is greater than p_s for any positive Q_f, a peak in S_{eff} with respect to Q_f does not occur. U_s is approximately proportional to p_s ($U_s \approx p_s S_{p0}$), and S_{eff} decreases monotonically with Q_f [Fig. 2(b)]. Upon texturing, p_s and U_s decrease considerably along a large portion of the surface compared to their values at the planar surface. Consequently, σ decreases below the surface area enhancement with Q_f, up to roughly 2×10^{10} cm^{-2}, at which point strong accumulation conditions start to prevail. For larger Q_f, σ increases and approaches the surface area enhancement, showing a similar trend with the case of negative Q_f.

In region III, strong inversion and strong accumulation conditions prevail for the large negative and positive Q_f, respectively. U_s is limited by the low concentration of carriers having the opposite polarity than the dielectric charge (e.g., n_s for a negative Q_f), and S_{eff} decreases with both positive and negative Q_f due to the reduction in these carrier concentrations. Upon texturing, carrier concentrations remain near constant along a large portion of the surface except in narrow regions that are close to the upper and bottom ends of the texture, as shown in Fig. 3. As a result, σ is approximately equal to the surface area enhancement [Figs. 2(c) and 2(d)].

Overall, the changes in the recombination rate upon texturing can be explained given the carrier distributions at the surfaces of textured and planar structures. Yet, the mechanisms governing the carrier concentration profiles in the first place need to be clarified. To build a more thorough understanding of these mechanisms that lead to the nonmonotonous relationship between σ and Q_f, we focus on the electrostatics in the SCR in the following section.

B. Electrostatics in textured and planar surfaces

Spatial distributions of carrier concentrations are approximately independent of recombination processes when the recombination rate is sufficiently small throughout the SCR and the quasi-Fermi levels (QFLs) of electrons and holes are near constant. In that case, the necessity to solve the continuity and drift-diffusion equations to calculate ψ and carrier concentrations is removed, and their profiles are governed mainly by electrostatics (i.e., the Poisson's equation). The constant QFL approximation is valid for the range of Q_f and for the structures considered in this work as discussed in the Appendix A. Therefore, analyzing the electrostatics of the SCR is sufficient to interpret the carrier concentration distributions, leading to the trends observed in σ.

Here, to analyze the textured structures in a simplified manner, we provide two approaches that are based on a parallel dielectric plate structure instead of the oblique texture considered in Sec. III A. The electrical conditions in between a parallel-plate structure are analogous to those in an oblique texture with an infinitely large aspect ratio and height, and we assume that these conditions are representative of those in an oblique texture with a finite height to a certain extent. The first approach, which is based on the solution of Poisson's equation, is presented in Appendix B. It provides a semianalytical groundwork while verifying that the carrier concentrations are indeed governed mainly by electrostatics. The second approach, which is presented in the following subsection, is based on the charged surface interaction model proposed by Gregory [31]. Following the author, we also name it the "compression model," yet the model is extended here to cover a wider range of band-bending conditions than the original work, which is based on weak band-bending conditions. Finally, we discuss the applicability of parallel-plate-based models, in general, to a texture with a finite height.

1. Compression model

A surface texture can be modeled as a parallel-plate structure where the dielectric plates at each end represent the opposing facets of the texture. Similarly, a semi-infinitely thick planar silicon can be considered as a parallel-plate structure with an infinitely large plate separation, yet we reserve the term "parallel-plate structure" specifically to refer to configurations with a finite plate separation (W). When the plate separation and the volume of silicon decrease from infinity to a finite value (e.g., when a texture is introduced), the surface-to-volume ratio of the structure increases. If the decrease in the volume of silicon also leads to a decrease in the volume of the SCRs (i.e., SCRs of the opposing facets overlap, $W < 2 \times d_{\mathrm{SCR}}$), free carriers of the semi-infinite structure that are left outside the confined volume are redistributed in between the plates [31]. Because of this redistribution, the total space charge induced in silicon, Q_{SC} ($= -Q_f$, neglecting the charge trapped in interface states), is compressed into a smaller volume, and the dielectric charge compensation occurs within a distance of $W/2$ from each one of the symmetrical plate surfaces. As a result, ρ increases throughout the silicon in between the plates. A schematic illustrating the distribution of ρ in semi-infinite and parallel-plate structures is shown in Fig. 5, where the yellow-filled areas underneath the dashed curves represent the carriers in the semi-infinite structure that are located outside the confined volume of the parallel structure, and the arrows represent

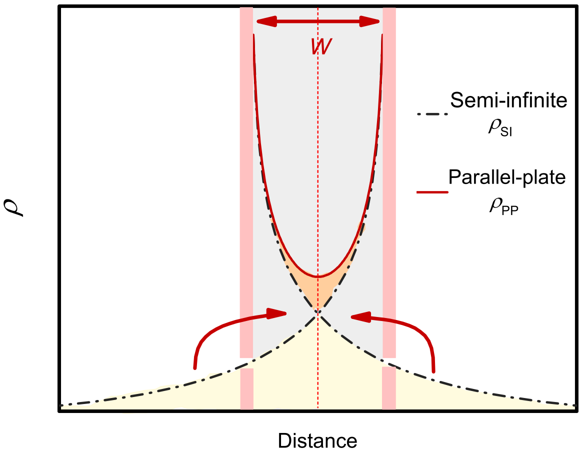

FIG. 5. Schematic representation of the net charge distribution in semi-infinite ($W = \infty$) (black dashed-dotted lines) and parallel-plate (red solid line) structures with arbitrary units for the distance and ρ. The yellow-filled areas under the curves represent the charge that is left outside the confinement volume in the semi-infinite structure and needs to be redistributed upon volume confinement. Red arrows symbolize the redistribution of charge in a smaller volume. Orange-filled areas underneath the curves represent the addition of the redistributed charge in the parallel-plate structure. Pink vertical columns represent the dielectric layers.

the carrier and space charge redistribution. Here, we denote ρ in the semi-infinite and parallel-plate structures by ρ_{SI} and ρ_{PP}, respectively, and the absolute change in ρ upon volume confinement is denoted by ρ_{RD} $(= \rho_{\mathrm{PP}} - \rho_{\mathrm{SI}})$.

The relative changes in n_s and p_s upon volume confinement in a parallel-plate structure depend on the spatial distribution of ρ prior to the confinement, ρ_{SI}, and W of the parallel plate. To quantify the depth where the majority of ρ_{SI} is located within, and to estimate the fraction of Q_{SC} that is redistributed upon volume confinement, we define a parameter, effective compensation depth (d_{eff}), which is formulated as

$$d_{\mathrm{eff}} = d[Q = Q(\infty)F], \tag{6}$$

$$Q(d) = \int_0^d \rho_{\mathrm{SI}}(y)\,dy, \tag{7}$$

where $Q(d)$ (in cm^{-2}) is the integration of ρ_{SI} within a depth of d into the silicon, and F is the fraction of Q_{SC} $[= Q(\infty)]$ within a depth of d_{eff} into silicon [i.e., $F = Q(d_{\mathrm{eff}})/Q_{\mathrm{SC}}$]. While a small d_{eff} corresponds to a large ρ_{SI} gradient from the surface into silicon and a localization of ρ_{SI} close to the surface, a large d_{eff} corresponds to a relatively smaller gradient in ρ_{SI} with the majority of ρ_{SI} spread out into the silicon. Figure 6 shows d_{eff} for $F = 0.63$ $(1 - e^{-1})$ and d_{SCR} [calculated according to Eq. (4)] for positive and negative Q_f for $\Delta n = 1 \times 10^{14}$ cm^{-3}. In addition, Fig. 7 shows the profiles of ρ_{SI}, where the filled areas underneath the curves indicate the regions where the $F = 0.63$ of Q_{SC} lie, for three positive Q_f values, 5×10^8, 2×10^{10}, and 2×10^{12} cm^{-2}, representing regions I, II, and III, respectively. Note that the choice of $F = 0.63$ is solely to be in accord with L_D at small Q_f, and analyzing for another F that correctly reflects the trends regarding the carrier population dynamics would still be legitimate. Moreover, the pink columns in Fig. 7 are representative of the dielectric layers at each end of the parallel plate structure with a $W = 100$ nm (i.e., the average separation length of oblique surfaces of the textured structures analyzed in Sec. III A), which is analyzed as an example.

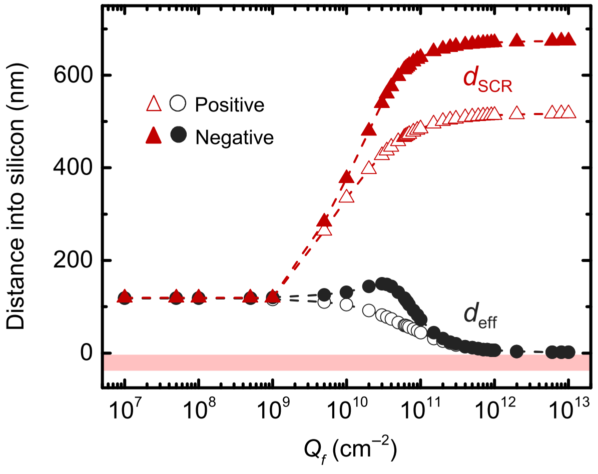

FIG. 6. Depth of the SCR (d_{SCR}) and effective compensation depth (d_{eff}) with $F = 0.63$ for negative and positive Q_f for the semi-infinite structure. The pink bold horizontal line indicates the position of the dielectric layer.

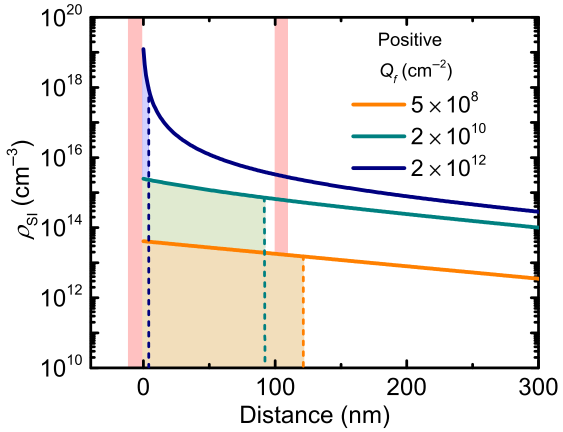

FIG. 7. Distributions of induced space charge densities in the semi-infinite structure (ρ_{SI}) for three positive Q_f values. Dashed lines indicate the location of d_{eff} and the filled areas under the distribution curves between the surface and d_{eff} highlight the regions where the fraction F of the induced charge lies. Pink vertical columns indicate the locations of dielectric plates for $W = 100$ nm.

In region I, where weak band-bending conditions prevail ($|\psi| \ll kT/q$), ρ_{SI} decays exponentially from the surface with a characteristic length approximately equal to L_D in the semi-infinite silicon for both negative and positive Q_f [i.e., $\rho_{\mathrm{SI}} = \rho_{\mathrm{SI},s} \exp(-y/L_D)$]. Yet, n_{SI} and p_{SI} throughout the SCR are approximately constant compared to their concentrations in the quasineutral base since ρ_{SI} is much smaller than n_{SI}. Since L_D is related to the spatially near-constant n_{SI} and p_{SI} through Eq. (1), the profile of ρ_{SI} remains independent of Q_f as long as weak band-bending conditions persist. Therefore, d_{eff} and d_{SCR} (≈ 120 nm) are approximately constant in this regime for both dielectric charge polarities (Fig. 6). Upon volume confinement in a parallel-plate structure with $W = 100$ nm, d_{eff} exceeds the width of the parallel-plate structure that needs to accommodate Q_{SC} (i.e., $W/2 = 50$ nm $< d_{\mathrm{eff}} = 120$ nm) as illustrated in Fig. 7 for a Q_f of 5×10^8 cm^{-2}. Accordingly, a relatively large portion of Q_{SC} is redistributed upon volume confinement, and $\rho_{\mathrm{PP},s}/\rho_{\mathrm{SI},s}$ $(= 1 + \rho_{\mathrm{RD},s}/\rho_{\mathrm{SI},s})$ is approximately equal to 2.5 [Figs. 8(a) and 8(b)]. However, since $\rho_{\mathrm{RD},s}$ is very low compared to $n_{\mathrm{SI},s}$ (e.g., $\rho_{\mathrm{RD},s} = 6.2 \times 10^{13}$ $\mathrm{cm}^{-3} \ll n_{\mathrm{SI},s} = 1.106 \times 10^{15}$ cm^{-3} for $Q_f = 5 \times 10^8$ cm^{-2}), the relative change in ρ_s is not reflected to those in n_s and p_s, and $n_{\mathrm{PP},s}/n_{\mathrm{SI},s}$ $(\approx 1 + \rho_{\mathrm{RD},s}/n_{\mathrm{SI},s})$ remains near unity. Overall, although d_{eff} is large compared to $W/2$, relative changes in free carrier concentrations upon volume confinement are negligible in this regime.

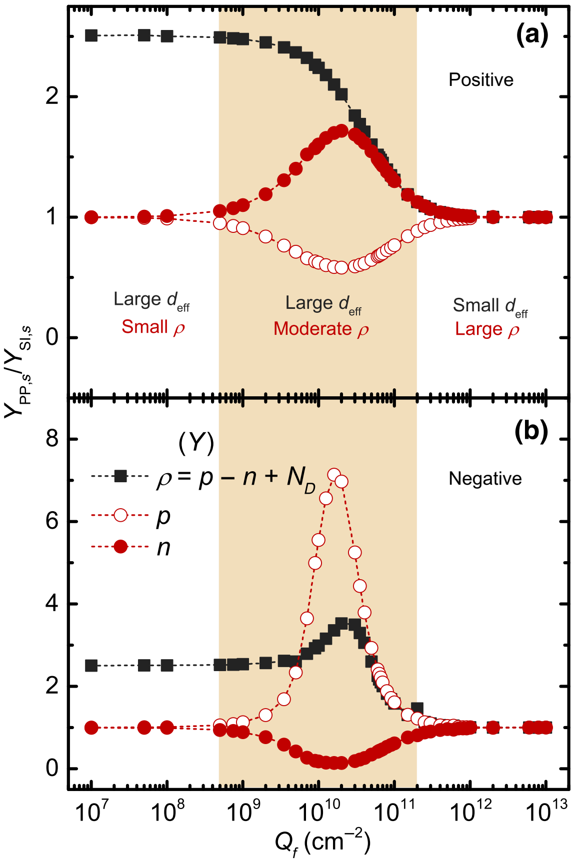

FIG. 8. Ratio of ρ, p, and n at the surface of a parallel-plate structure with $W = 100$ nm to those at the surface of the semi-infinite structure, with respect to (a) positive and (b) negative Q_f. The variable Y is a placeholder that represents either ρ, p, or n as provided in the legend.

For moderately large positive Q_f in region II, dielectric charge compensation is achieved by the free electrons accumulating near the surface. Whereas $\rho_{\mathrm{SI},s}$ and d_{SCR} increase with Q_f, d_{eff} decreases. With the decrease in d_{eff}, the portion of Q_{SC} that is redistributed upon volume confinement reduces and $\rho_{\mathrm{RD},s}$ becomes less significant compared to $\rho_{\mathrm{SI},s}$. Consequently, $\rho_{\mathrm{PP},s}/\rho_{\mathrm{SI},s}$ $(1 + \rho_{\mathrm{RD},s}/\rho_{\mathrm{SI},s})$ decreases with Q_f [Fig. 8(a)]. On the other hand, $\rho_{\mathrm{RD},s}$ increases with Q_f and eventually becomes comparable to $n_{\mathrm{SI},s}$. In other words, the redistributed charge density becomes sufficiently large to affect the carrier concentrations at the surface upon volume confinement. As a result, $n_{\mathrm{PP},s}/n_{\mathrm{SI},s}$ increases and approaches the decreasing $\rho_{\mathrm{PP},s}/\rho_{\mathrm{SI},s}$, up to a Q_f of around 2×10^{10} cm^{-2}. For a larger Q_f ($> 2 \times 10^{10}$ cm^{-2}), $n_{\mathrm{PP},s}/n_{\mathrm{SI},s}$ converges to $\rho_{\mathrm{PP},s}/\rho_{\mathrm{SI},s}$ and both decrease with Q_f as free carrier localization becomes prevalent. Overall, the interplay between the increase in the effectiveness of the $\rho_{\mathrm{RD},s}$ on free carrier concentrations and the decrease in d_{eff} with increasing Q_f results in the peak in $n_{\mathrm{PP},s}/n_{\mathrm{SI},s}$ near a Q_f of 2×10^{10} cm^{-2}.

For a moderately large negative Q_f in region II, a depletion region is induced in the semi-infinitely thick silicon. Because of the limited concentration of spatially fixed ionized donors and free holes in silicon, both d_{SCR} and d_{eff} increase with Q_f to compensate the dielectric charges (Fig. 6) (i.e., for 1×10^9 cm^{-2} $< Q_f < 3 \times 10^{10}$ cm^{-2}). The increase continues until high concentrations of holes ($p > N_D$) build up near the surface (i.e., near $Q_f \approx 3 \times 10^{10}$ cm^{-2}), at which point d_{SCR} approximately saturates and d_{eff} decreases for larger Q_f [Fig. 8(b)]. Upon volume confinement, the interior of silicon becomes completely depleted for a Q_f approximately equal to $N_D W/2$ ($= 2.5 \times 10^9$ cm^{-2}), reaching the limit of dielectric charge compensation that can be provided by ionized donors. Then, excess amounts of holes are generated to compensate Q_f and a premature switch to the inversion regime occurs. As a result of this abrupt change from depletion to inversion conditions, the relative changes in p_s and n_s are more pronounced compared to those observed with a similarly large positive Q_f (Fig. 8). Note that this abrupt change in carrier concentrations at $Q_f = N_D W/2$ is more pronounced under dark conditions where the asymmetry between n_s and p_s is much larger prior to volume confinement. For clarity, the results for this case are also provided in Appendix B.

In region III, the distribution of ρ_{SI} is similar close to the surface for both polarities of large Q_f ($> 2 \times 10^{11}$ cm^{-2}). The very large $\rho_{\mathrm{SI},s}$ ($\approx -n_s$ or p_s) rapidly decays from the surface into silicon. More than an order of magnitude difference in ρ_{SI} arises between the surface and a location only a few nanometers deep into silicon, as illustrated in Fig. 7 for a positive Q_f of 2×10^{12} cm^{-2}. Then, the majority of the dielectric charge compensation occurs in this narrow region of high free carrier concentration. As shown in Fig. 6, d_{eff} is reduced to below a few nm, while d_{SCR} stays approximately constant near 700 nm. Upon volume confinement, the majority of the induced space charge in silicon remains undisturbed since d_{eff} is much smaller than $W/2$. Those that are redistributed into the confined volume have approximately no effect on the very large free carrier concentration near the surface (i.e., $\rho_{\mathrm{RD},s}/n_{\mathrm{SI},s} \ll 1$). As a result, $n_{\mathrm{SI},s}$ and $p_{\mathrm{SI},s}$ remain approximately unchanged (i.e., $n_{\mathrm{PP},s}/n_{\mathrm{SI},s} \approx p_{\mathrm{PP},s}/p_{\mathrm{SI},s} \approx 1$) [Figs. 8(a) and 8(b)].

The aforementioned carrier compression and redistribution mechanisms can be translated into relatively simple mathematical formulations that can justify the arguments of the compression model and provide an alternative path to the solution of Poisson's equation to calculate the relative changes in carrier concentrations. Three main assumptions simplify the calculations considerably: (i) $\rho_{\mathrm{SI},s}$ is constant between the surface and a distance d_{eff} into silicon; (ii) $\rho_{\mathrm{SI},s}$ decays exponentially with a characteristic length of L_D for $y > d_{\mathrm{eff}}$ [i.e., $\rho_{\mathrm{SI}} = \rho_{\mathrm{SI}}(d_{\mathrm{eff}}) \exp(-y/L_D)$]; and (iii) the portion of Q_{SC} in the semi-infinite silicon that is located outside the region allocated to the induced charge in the parallel-plate structure (i.e., $y > W/2$) is redistributed uniformly in between $y = 0$ and $y = W/2$ upon volume confinement. The first assumption results in an approximation for $\rho_{\mathrm{SI},s}$ as

$$\rho_{\mathrm{SI},s} \approx -\frac{Q_f F}{d_{\mathrm{eff}}}. \tag{8}$$

Combining the second and third assumptions yields an approximation for $\rho_{\mathrm{RD},s}$ as

$$\rho_{\mathrm{RD},s} \approx -\frac{Q_f(1-F)}{W} \exp\left(\frac{d_{\mathrm{eff}} - W/2}{L_D}\right). \tag{9}$$

Combining Eqs. (8) and (9), $\rho_{\mathrm{PP},s}/\rho_{\mathrm{SI},s} = 1 + \rho_{\mathrm{RD},s}/\rho_{\mathrm{SI},s}$ (denoted here as M_s) can be approximated as

$$M_s \approx 1 + \frac{2d_{\mathrm{eff}}(1-F)}{WF} \exp\left(\frac{d_{\mathrm{eff}} - W/2}{L_D}\right). \tag{10}$$

M_s is reflected onto the changes in n_s and p_s through the factor we denote as K_s [$n_{\mathrm{PP},s}/n_{\mathrm{SI},s} = (p_{\mathrm{PP},s}/p_{\mathrm{SI},s})^{-1}$], with the relationship

$$M_s \rho_{\mathrm{SI},s} = K_s^{-1} p_{\mathrm{SI},s} - K_s n_{\mathrm{SI},s} + N_D. \tag{11}$$

Finally, considering that $(pn)_{\mathrm{SI},s}$ product is constant regardless of Q_f, and $p_{\mathrm{SI},s}$ and $n_{\mathrm{SI},s}$ are related to each other through Eq. (8), solving Eq. (11) for K_s yields

$$K_s \approx \frac{N_D + \dfrac{Q_f F M_s}{d_{\mathrm{eff}}} + \sqrt{\left(N_D + \dfrac{Q_f F M_s}{d_{\mathrm{eff}}}\right)^2 + 4(pn)_{\mathrm{SI},s}}}{N_D + \dfrac{Q_f F}{d_{\mathrm{eff}}} + \sqrt{\left(N_D + \dfrac{Q_f F}{d_{\mathrm{eff}}}\right)^2 + 4(pn)_{\mathrm{SI},s}}}. \tag{12}$$

Provided that d_{eff} and F are known for a chosen Q_f, the relative changes in ρ_s, n_s, and p_s can be roughly estimated using Eqs. (10) and (12). Figure 9 illustrates the comparison of the simulation results and calculations of $n_{\mathrm{PP},s}/n_{\mathrm{SI},s}$ and $p_{\mathrm{PP},s}/p_{\mathrm{SI},s}$ based on Eq. (12). Overall, the nonmonotonous nature of $n_{\mathrm{PP},s}/n_{\mathrm{SI},s}$ and $p_{\mathrm{PP},s}/p_{\mathrm{SI},s}$ with respect to Q_f is captured in the model with a reasonable accuracy in regions I and III and with a more pronounced deviation from the simulation results in region II. Note that better matches between the model and simulation results can be obtained by adjusting the choice of F, and therefore d_{eff}, for specific electrical and geometrical configurations.

2. Applicability and limitations of parallel-plate models

Analyzing surface textures as parallel-plate structures is relatively simple, but there are certain limitations on the applicability of formulations [e.g., Eq. (12)] that are based on them to a multidimensional texture with a finite height. To clarify the range of applicability and practical uses of these models, we compare the relative changes in free carrier concentrations upon geometrical modifications for oblique and parallel-plate structures. We assume that $p_{\mathrm{textured},s}/p_{\mathrm{planar},s}$ and $n_{\mathrm{textured},s}/n_{\mathrm{planar},s}$ at a location on an oblique facet can be approximated by the $p_{\mathrm{PP},s}/p_{\mathrm{SI},s}$ and $n_{\mathrm{PP},s}/n_{\mathrm{SI},s}$ of a parallel plate with W equal to the lateral separation between the oblique facets (denoted as w) at that particular location as in

$$\frac{p_{\mathrm{textured},s}(h)}{p_{\mathrm{planar},s}} \approx \frac{p_{\mathrm{PP},s}[w(h)]}{p_{\mathrm{SI},s}}, \tag{13}$$

where h is the distance along the surface where the origin is located at the bottom end of the surface.

A comparison of $p_{\mathrm{textured},s}/p_{\mathrm{planar},s}$ that is (i) extracted from simulations of an oblique texture with a finite height [Fig. 1(b)], (ii) calculated from $p_{\mathrm{PP},s}/p_{\mathrm{SI},s}$, which is extracted from simulations of parallel-plate structures (Fig. 5); and (iii) calculated from $p_{\mathrm{PP},s}/p_{\mathrm{SI},s}$, which is approximated according to Eq. (12), is shown in Fig. 10 for $Q_f = 5 \times 10^{10}$ cm^{-2}. Along a large portion of the oblique surface, the three results agree with one another. Yet, $p_{\mathrm{textured},s}/p_{\mathrm{planar},s}$ is underestimated in parallel-plate

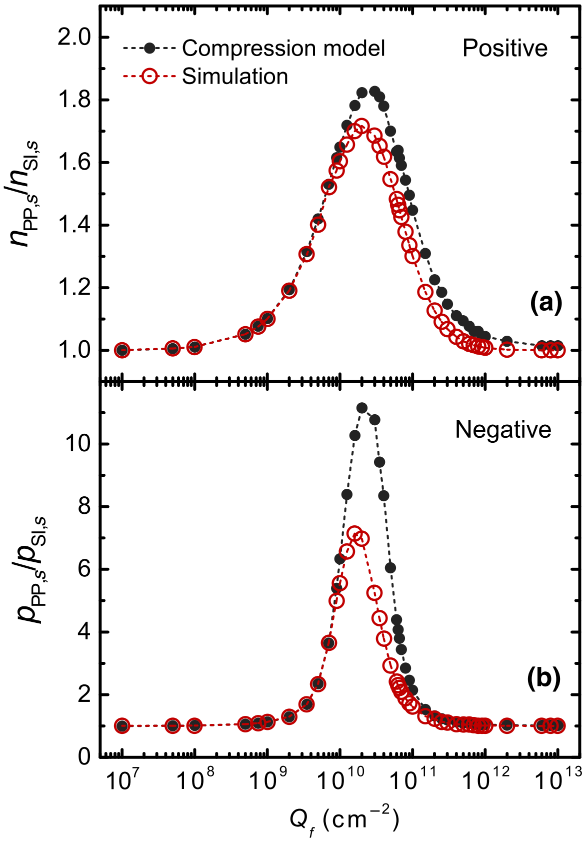

FIG. 9. Comparison of the $n_{\mathrm{PP},s}/n_{\mathrm{SI},s}$ and $p_{\mathrm{PP},s}/p_{\mathrm{SI},s}$ obtained from the compression model (black filled circles) and fully numerical simulations (red hollow circles) for $W = 100$ nm.

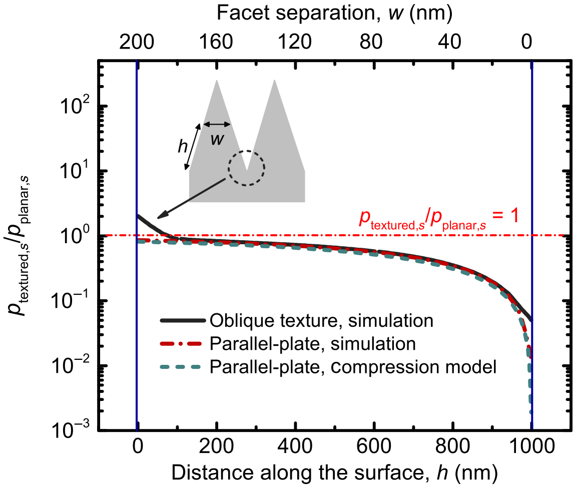

FIG. 10. A comparison of $p_{\text{textured},s}/p_{\text{planar},s}$ along an oblique texture facet and those obtained from parallel-plate simulations and from calculations based on the equations derived from the compression model where the plate separation, $w(h)$, is assumed to be equal to the lateral facet separation of the oblique texture at that particular location. Q_f is positive and equal to 5×10^{10} cm^{-2}. The region where a local surface-to-volume reduction results in a $p_{\text{textured},s}/p_{\text{planar},s}$ greater than unity is indicated by the dashed circle in the gray-colored schematic of the texture. The vertical dark blue lines mark the bottom and top ends of the texture surface.

configurations at locations that are very close to the top and bottom ends of the texture facet. In both regions, the volume available for dielectric charge compensation is underestimated with the parallel-plate models. At the top end of the texture where the opposing facet ends meet, $w(0)$ is equal to 0 according to the parallel-plate models, meaning that there is no volume in silicon for dielectric charge compensation. However, this is not the case physically, and these models fail near this location where $n_{\text{PP},s}/n_{\text{SI},s}$ and $p_{\text{PP},s}/p_{\text{SI},s}$ approach to infinity and 0, respectively. On the other hand, near the bottom end of the texture, a clear deviation from the volume compression assumption is observed. The volume available for dielectric charge compensation locally expands near the sharp bottom end, leading to a local reduction in the surface-to-volume ratio. This leads to a degraded field-effect passivation compared to that observed in a planar structure and $p_{\text{textured},s}/p_{\text{planar},s}$ becomes larger than unity near the bottom end. This local decrease in the surface-to-volume ratio contradicts the volume compression assumption inherent to a parallel-plate-based model. Since the volume in silicon that is allocated to the SCRs of the opposing facets of a parallel-plate cannot get any larger than the volume available in the semi-infinite configuration, the volume expansion at the bottom end of the texture is not captured by these models.

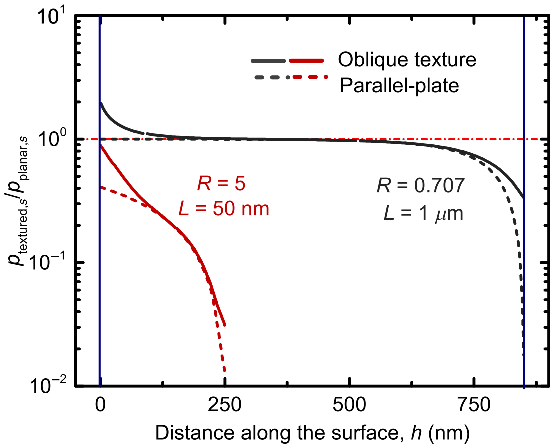

FIG. 11. A comparison of $p_{\text{textured},s}/p_{\text{planar},s}$ attained from simulations of oblique textures and calculations based on the simulations of parallel-plate structures, as in Eq. (13), for different texture geometries having a positive $Q_f = 5 \times 10^{10}$ cm^{-2}.

As indicated by the local variations in the surface-to-volume ratio along the surface of the texture, the applicability of parallel-plate models is influenced considerably by the geometry of the texture. In particular, deviations from parallel-plate assumption arise when either one of the two geometrical characteristics is present in the oblique texture; when the length of the texture facet is very small so that the effects of expansion and compression overlap, and when R is small so that the assumption of facets being parallel to each other is not very realistic. Figure 11 shows $p_{\text{textured},s}/p_{\text{planar},s}$ for two structures where the error observed with a parallel-plate model is relatively large: a texture with $L = 50$ nm and $R = 5$ and a texture with $L = 1$ μm and $R = 0.7$. For the smaller texture of the two, underestimation of $p_{\text{textured},s}/p_{\text{planar},s}$ is more significant than that observed for large textures since the parallel-plate model does not take into account the local surface-to-volume expansion near the bottom end, and this mechanism is effective in a relatively large portion of the short surface. Besides, carrier concentrations at an oblique surface gradually converge to those in a planar surface as a texture becomes smaller. However, this aspect is also not captured in parallel-plate models and the underestimation of $p_{\text{textured},s}/p_{\text{planar},s}$ becomes more pronounced with decreasing period (data not shown). In that case, parallel-plate models are no longer applicable in the form they are used in this study. For the larger texture (i.e., $L = 1$ μm and $R = 0.7$), the difference between oblique texture simulations and calculations based on parallel-plate simulations is not as significant. Yet, near the top of the texture, the difference is still higher than that observed with high-aspect-ratio textures.

C. The choice of passivation method and material

Field-effect passivation can be classified under two main groups as intrinsic and extrinsic [32]. Whereas intrinsic

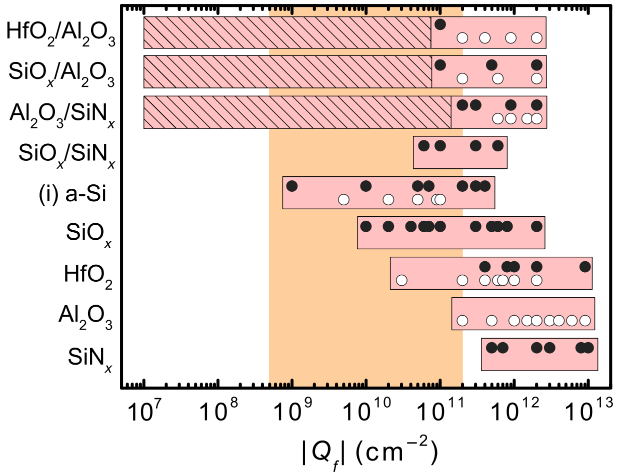

FIG. 12. Materials that are commonly used to passivate silicon surfaces and the associated Q_f values reported in the literature for planar surfaces. The filled and open circle markers indicate the positive and negative Q_f, respectively. Boxes filled with oblique lines indicate the range of Q_f that is expected to be accessible with zero-charge stacks. The colored region between a Q_f of 5×10^8 to 2×10^{11} cm^{-2} indicates the range where the modification in field-effect passivation upon texturing is relatively significant.

passivation relies on the charge generated in the films during the depositions, extrinsic passivation is used to modify the effective Q_f, typically by utilizing a corona-charge device following the film depositions [32–39].

Considering intrinsic passivation, Fig. 12 illustrates a set of commonly used materials and the associated Q_f values reported in the literature. For silicon, some of the most commonly used single-layer passivating materials have been SiO_x [17,40–46], SiN_x:H [47–50], Al_2O_3 [47,51–54], and intrinsic (i) a-Si:H [55–58] (":H" in hydrogenated films is omitted for brevity later in the text). HfO_2 is also worth mentioning due to the tunability in both the polarity and magnitude of Q_f by varying process parameters, which is rather rare among passivating dielectrics [59–64]. Similarly, a difference in charge polarity is observed for (i) a-Si films due to the amphoteric interface states near the (i) a-Si/c-Si interface [56,57]. With multilayer passivation, the effective Q_f can be modified by varying the layer thicknesses since different densities and polarities of charges can accumulate at different locations in a stack [65–67]. Whereas solely the magnitude of the effective Q_f is changed with stacks such as SiO_x/SiN_x [68–70], the polarity can also be modified with stacks such as SiO_x/Al_2O_3 [45,71,72], Al_2O_3/SiN_x [73,74], and HfO_2/Al_2O_3 [46,75]. Capable of providing both low Q_f and defect density, the latter configurations are also referred to as "zero-charge" stacks [72,75]. However, very low Q_f values associated with zero-charge stacks have not been experimentally demonstrated so far, possibly due to sensitivity limitations of the utilized measurement techniques [71,74]. To mark this uncertainty in Q_f, the range extending to very low Q_f values is indicated by oblique dashes for these stacks in Fig. 12. Overall, while single-layer (i) a-Si, thermally grown SiO_2, and HfO_2 passivated surfaces with moderate Q_f appear more susceptible to a change in field-effect passivation upon texturing, negligible change is expected for Al_2O_3 and SiN_x passivated surfaces with high Q_f. Additionally, the range of attainable Q_f is significantly extended with multilayer stacks, which may allow it to benefit more easily from an optimized field-effect passivation.

Considering extrinsic field-effect passivation, to our knowledge, corona-charge deposition on dielectrics has been the only technique that was pursued for solar cell applications. The limits of Q_f are limited by factors such as the rate of charge deposition, the dielectric strength, and the degradation that may occur in chemical passivation [38,76–78]. Although this technique has been used mainly for electrical characterization of dielectric interfaces [79,80], it has the potential to be more widely utilized in cell fabrication with recent advances in maintaining the deposited charge over extended periods [32,35–39,81]. Overall, extrinsic passivation offers a flexible route to adjust Q_f, with the potential to be integrated into already established intrinsic passivation schemes.

The ability to tailor Q_f through both intrinsic and extrinsic passivation provides opportunities to maximize the benefit from field-effect passivation in textured surfaces. Yet, it should be noted that this maximum benefit (i.e., minimum attainable S_{eff}) may not necessarily correlate with a low σ. Considering the stronger dependence of S_{eff} to Q_f as compared to σ, one may ultimately choose to aim for large Q_f regardless of the surface geometry. Furthermore, σ is based on the assumption that Q_f is the same for textured and planar surfaces, which was demonstrated to be approximately the case for random pyramid textured samples for some dielectrics [5,82]. However, it is not certain if this assumption is applicable to every surface morphology and passivating material. Since S_{eff} has a strong dependency on Q_f (e.g., Q_f^{-2} for large Q_f [83]), a violation in constant Q_f assumption can lead to significant differences in field-effect passivation, which should not be mistaken with the geometrical effects (i.e., σ).

D. Effect of experimental error on σ

S_{eff} can be calculated precisely in a simulation domain with the exact knowledge of recombination rate at every location of the simulated structures [see Eq. (5)]. However, this knowledge is not always available in experiments, and one may have to utilize certain assumptions for the calculation. For example, one commonly used formulation to calculate S_{eff} from photoconductance decay measurements (assuming identical passivation at each side of the measured sample) is

$$S_{\mathrm{eff}} = \frac{d_{\mathrm{total}}}{2}\left(\frac{1}{\tau_{\mathrm{eff}}} - \frac{1}{\tau_{\mathrm{bulk}}}\right), \tag{14}$$

where d_{total} is the wafer thickness; τ_{eff} is the effective lifetime, which is a combination of both surface and bulk recombination within the sample; and τ_{bulk} is the bulk lifetime of the sample, which is a combination of Auger, SRH, and radiative recombination mechanisms. Assuming a spatially uniform Δn and τ_{bulk} throughout the sample, Eq. (14) is, in fact, analogous to Eq. (5). Yet, the accuracy of a calculation based on Eq. (14) depends on the exact knowledge of τ_{bulk}, which may not be available. Some of the common practices in case of improper knowledge of τ_{bulk} are (i) assuming it is infinitely large, where the obtained S_{eff} corresponds to an upper limit, and (ii) using an intrinsic recombination model, assuming negligible extrinsic (SRH) recombination. However, specifically for low S_{eff}, which is likely to be observed for well-passivated planar surfaces, the relative error associated with the calculation of S_{eff} [i.e., $(S_{\mathrm{eff,actual}} - S_{\mathrm{eff,calculated}})/S_{\mathrm{eff,actual}}$] can be significant. Consequently, σ calculated from these S_{eff} values may deviate significantly from the actual value.

To demonstrate the effect of a calculation error in S_{eff} on σ, we consider three cases that can be observed in an experiment. We assume $N_D = 1 \times 10^{15}$ cm^{-3} as in the previous sections and, hence, an upper limit for τ_{bulk} at around 110 ms for $\Delta n = 1 \times 10^{14}$ cm^{-3}, calculated from Richter's intrinsic recombination model [24]. For all three cases, d_{total} is 300 μm and the actual σ is 10, but the actual S_{eff} and τ_{bulk} values are different. First, τ_{eff} values for textured and planar structures are calculated inserting the specified d_{total}, S_{eff}, and τ_{bulk} values into Eq. (14). Then, we assume that these τ_{eff} values are measurement readings and τ_{bulk} is a user input necessary to calculate the S_{eff} values through Eq. (14), where we vary the assumed τ_{bulk} from 1 up to 400 ms (which can be regarded close to the infinite lifetime assumption).

Figure 13 shows the calculated σ versus assumed τ_{bulk} for the three cases. For an actual τ_{bulk} of 10 ms, both infinite and intrinsic lifetime assumptions for τ_{bulk} result in a calculated σ around 4.5, whereas it is, in fact, 10 (i.e., 55% relative error). Similarly, for an actual τ_{bulk} of 30 ms, the calculated σ is underestimated with a relative error of around 25% for both assumptions. On the other hand, the error in σ is less than 5% for both assumptions when $S_{\mathrm{eff,planar}} = 10$, and τ_{eff} is much smaller compared to τ_{bulk} for both textured and planar structures. Overall, despite the quite large actual τ_{bulk} values over 10 ms, the difference between calculated and actual σ can be considerable, especially for low $S_{\mathrm{eff,planar}}$. These artificially low σ values can lead to the perception of an enhanced field-effect passivation in the textured structures when there is, in fact, no considerable difference. Particularly for high passivation configurations, such error should be avoided by extracting τ_{bulk} as precisely as possible [84] or by using a performance parameter other than S_{eff} [83].

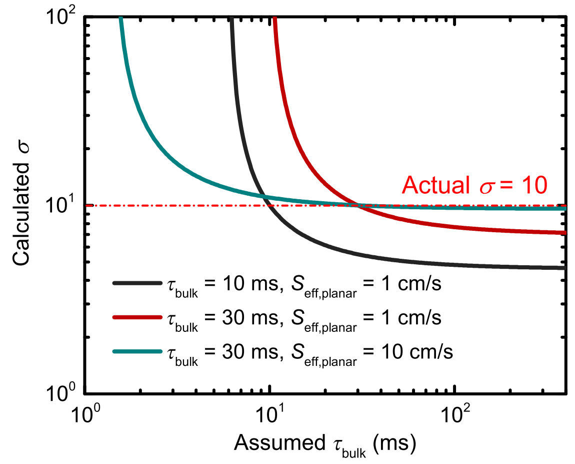

FIG. 13. σ calculated from S_{eff} values calculated according to Eq. (14) for three different cases with different actual τ_{bulk} and $S_{\mathrm{eff,textured}} = \sigma S_{\mathrm{eff,planar}}$ values, where the actual $\sigma = 10$ is fixed for all cases. First, the hypothetical measurement reading τ_{eff} is calculated using the actual τ_{bulk} and S_{eff} values. Then, S_{eff} and consequently the σ values are calculated with various τ_{bulk} assumptions.

IV. CONCLUSIONS

Numerical analysis of field-effect passivation of planar and textured surfaces reveals a nonmonotonous relation between σ and Q_f for a constant Δn in the quasineutral base. Carrier concentrations at the surface of structures having a moderately large Q_f appear to be influenced more significantly from geometrical modifications than those having small or large Q_f. Analyzing the electrostatics of interacting SCRs of opposing surfaces, we show that the parameter d_{eff}, introduced in this study, is a major determinant in this nonmonotonous behavior. In particular, the small d_{eff} associated with the large Q_f corresponds to a localization of carriers close to the surface, which results in relatively minor changes in carrier concentrations along a large portion of the surface upon texturing. Additionally, it is shown that simplified models that are based on parallel-plate structures can be used to interpret and estimate the relative changes in carrier concentrations along the surface of oblique textures.

In the analysis, we assume that the interface parameters are independent of surface geometry. Therefore, the presented results regarding σ, in fact, serve as a reference to what can be expected in an experimental scenario where the interface parameters indeed remain the same upon texturing. Deviations in experimental measurements of σ from these results are expected to provide guidance in the identification of differences between the interface parameters of textured and planar surfaces.

ACKNOWLEDGMENTS

Funding provided by TUBITAK through the project with Grant No. 116F104 is gratefully acknowledged. The authors thank Sören Schäfer and Sarah Kajari-Schröder for valuable discussions.

APPENDIX A: VALIDITY OF CONSTANT QUASI-FERMI-LEVEL ASSUMPTION

For $S_{n0} = 5 \times 10^3$ cm/s, the maximum difference in the QFLs for electrons and holes throughout the SCR (i.e., $|\Delta E_{Fn}|$ and $|\Delta E_{Fp}|$, respectively) are smaller than 0.2 meV for the textured structures with a positive Q_f. These differences are similar for a negative Q_f, except in region II where a peak of roughly 2 meV is reached for configurations with very large U_s (e.g., for a negative $Q_f = 2 \times 10^{10}$ cm^{-2}). Overall, since $|\Delta E_{Fn}|$ and $|\Delta E_{Fp}|$ are much smaller than the thermal energy of the free carriers ($kT \approx 26$ meV at 300 K), the constant QFL assumption can be regarded as reasonable.

To determine whether the nonmonotonous relationship between Q_f and σ differs for surfaces with varying passivation qualities and to check the applicability limits of constant QFL approximation, S_{n0} is varied (keeping $S_{n0}/S_{p0} = 100$) for a negative Q_f as shown in Fig. 14. Whereas for a relatively small $S_{n0} = 1 \times 10^3$ cm/s, $|\Delta E_{Fn}|$ and $|\Delta E_{Fp}|$ peak near 1 meV, for a higher $S_{n0} = 1 \times 10^3$ cm/s, they reach up to 25 meV, where $S_{\mathrm{eff,textured}}$ is the largest. However, trends regarding σ change only slightly and the constant QFL approximation remains feasible. For larger S_{n0}, the constant QFL approximation starts to fail, yet these S_{n0} values correspond to a rather poor interface passivation than what is practically achievable in most cases.

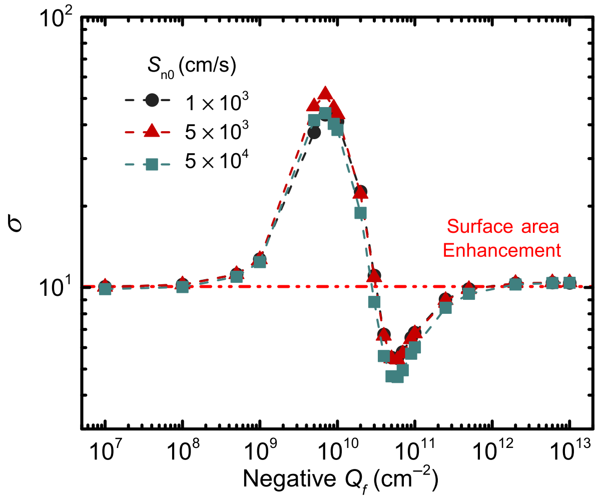

FIG. 14. σ vs Q_f for various S_{n0}, where $R = 5$. The red horizontal line indicates the surface area enhancement.

APPENDIX B: SOLUTION TO POISSON'S EQUATION FOR A PARALLEL-PLATE STRUCTURE UNDER ILLUMINATION

Assuming Boltzmann statistics for carrier concentrations, Poisson's equation is expressed in the one-dimensional form as

$$\frac{d^2\psi}{dy^2} = -\frac{qn_i}{\epsilon_s}\left[e^{q(\phi_{Fp}-\psi)/kT} - e^{q(\psi-\phi_{Fn})/kT} + \frac{N_D - N_A}{n_i}\right], \tag{B1}$$

where $\phi_{Fn} = (kT/q)\ln(n_i/n)$ and $\phi_{Fp} = (kT/q)\ln(p/n_i)$ are the quasi-Fermi potentials for electrons and holes, respectively. Neglecting the charge in the interface traps (i.e., $Q_f + Q_{\mathrm{SC}} = 0$), Gauss's law and the symmetry in the parallel-plate structure impose the boundary conditions

$$\frac{d\psi_s}{dy} = \frac{qQ_f}{\epsilon_s}, \tag{B2}$$

$$\frac{d\psi_0}{dy} = 0, \tag{B3}$$

where ψ_s is the electrostatic potential at $y = -W/2$ and $y = -W/2$, and ψ_0 is the electrostatic potential at $y = 0$. Using the relation $d^2\psi/dy^2 = [d(d\psi/dy)^2/d\psi]/2$ for the left-hand side of Eq. (B1) and integrating between $y = 0$ and $y = W/2$ in combination with Eq. (B2) yields

$$qQ_f = \sqrt{2kTn_i\epsilon_s}\Big[e^{q(\psi_s-\phi_{Fn})/kT} - e^{q(\psi_0-\phi_{Fn})/kT} + e^{-q(\psi_s-\phi_{Fp})/kT} - e^{-q(\psi_0-\phi_{Fp})/kT} - \frac{q(\psi_s-\psi_0)}{kT}\left(\frac{N_D - N_A}{n_i}\right)\Big]^{1/2}. \tag{B4}$$

The solution of Eq. (B4) requires numerical iteration, which was provided in previous works (including the charge trapped at the interface states) for both dark and illuminated cases for an infinitely thick base with $\psi_0 = 0$ [17,85]. However, ψ_0 is nonzero for a parallel-plate structure and Eq. (B4) needs to be solved for two unknowns (ψ_s and ψ_0). Therefore, a set of at least two equations is required to calculate ψ_s.

The electrical conditions induced in silicon due to fixed dielectric charges are analagous to those created by a voltage applied to the gate of a metal-oxide-semiconductor (MOS) structure. Here, we follow the works on undoped [86] and doped [87,88] double-gate MOS field-effect transistors (DG MOSFETs) with a focus on the analyses of ψ.

Assuming an undoped silicon and a positive Q_f, where $n \gg p$, Poisson's equation in Eq. (B1) reduces to

$$\frac{d^2\psi}{dy^2} = \frac{qn_i}{\epsilon_s} e^{q(\psi-\phi_{Fn})/kT}. \tag{B5}$$

Utilizing the same conversion used for $d^2\psi/dy^2$ to obtain Eq. (B4) and integrating Eq. (B5) twice between $y = 0$ and an arbitrary y in silicon yields [86]

$$\psi(y) = \phi_{Fn} - \frac{2kT}{q}\ln\left(\frac{W}{2\beta}\sqrt{\frac{q^2 n_i}{2\epsilon_s kT}}\cos\frac{2\beta y}{W}\right), \tag{B6}$$

where

$$\beta = \frac{W}{2}\sqrt{\frac{q^2 n_i}{2\epsilon_s kT}} e^{q(\psi_0-\phi_{Fn})/2kT}. \tag{B7}$$

As shown by Jin *et al.* [87], the solution in Eq. (B6) can be inserted as a first order approximation to a simplified form of Poisson's equation where one type of carrier is neglected, but the dopant concentration is not. Consequently, solutions for ψ were attained for semiconductors that are either fully depleted [87] or under accumulation [88]. However, in our case, ψ cannot be attained for the complete range of positive and negative Q_f when one type of carrier is neglected. Here, we insert Eq. (B6) as a first-order approximation to the complete form of Poisson's equation in Eq. (B1), taking into account both holes and electrons. Integrating both sides of Eq. (B1) with respect to y, with the boundary conditions in Eqs. (B2) and (B3), yields

$$\frac{d\psi}{dy} = -\frac{q}{\epsilon_s}\left[\frac{q^2 n_i^2 W^2 e^{q(\phi_{Fp}-\phi_{Fn})/kT}}{64\beta^3\epsilon_s kT}\left(\sin\frac{4\beta y}{W}+\frac{4\beta y}{W}\right) - \frac{4\beta\epsilon_s kT}{Wq^2}\tan\frac{2\beta y}{W} + (N_D - N_A)\,y\right]. \tag{B8}$$

Finally, integrating Eq. (B8) between $y = 0$ and an arbitrary y, we obtain

$$\psi(y) = \phi_{Fn} - \frac{2kT}{q}\ln\left(\frac{W}{2\beta}\sqrt{\frac{q^2 n_i}{2\epsilon_s kT}}\cos\frac{2\beta y}{W}\right) - \frac{q^3 n_i^2 W^4 e^{q(\phi_{Fp}-\phi_{Fn})/kT}}{256\beta^4\epsilon_s^2 kT}\left(1-\cos\frac{4\beta y}{W}+\frac{8\beta^2 y^2}{W^2}\right) - \frac{q\,(N_D - N_A)\,y^2}{2\epsilon_s}. \tag{B9}$$

The iterative solution of Eqs. (B2) and (B8) results in a Q_f-dependent β, which can be inserted into Eq. (13) to find the spatial distribution of ψ. The attained ψ can be used to calculate the n and p at the location of interest. In this respect, Fig. 15 shows the comparisons of $n_{\mathrm{PP},s}/n_{\mathrm{SI},s}$ and $p_{\mathrm{PP},s}/p_{\mathrm{SI},s}$ that are extracted from simulations conducted by ATLAS and those that are calculated by the numerical iteration of Eqs. (B4) and (B9), for $W = 100$ nm, both in the dark and under illumination. Note that the values of $n_{\mathrm{PP},s}$ and $p_{\mathrm{PP},s}$ are calculated by solving Eq. (B9) at $y = W/2$. However, a major limitation of Eq. (B9) is that it is not applicable for structures with large W (roughly > 300 nm) where the overlap of SCRs of opposing facets is insignificant. Therefore, it cannot be used to calculate $n_{\mathrm{SI},s}$ and $p_{\mathrm{SI},s}$, and to calculate these variables, Eq. (B4) is solved here for $\psi_0 = 0$. Overall, the simulation results and solution of Poisson's equation agree with each other (Fig. 15) and validate the nonmonotonous relationship between Q_f and relative changes in carrier concentrations.

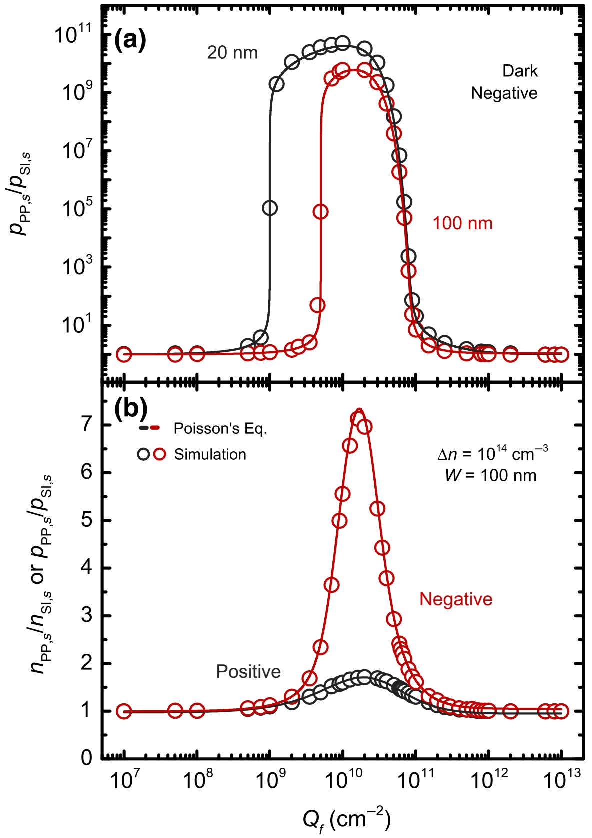

FIG. 15. Comparison of ratios of carrier concentrations at the surface of parallel-plate structures to those at the surface of the semi-infinite structure based on simulations conducted by ATLAS and from numerical iterations based solely on Eq. (B9) with $y = W/2$. The comparisons are shown for (a) negative Q_f in the dark for $W = 20$ nm and $W = 100$ nm and for (b) both negative and positive Q_f under illumination for $W = 100$ and $\Delta n = 1 \times 10^{14}$ cm^{-3}. For the illuminated case, $n_{\mathrm{PP},s}/n_{\mathrm{SI},s}$ is shown for the positive Q_f and $p_{\mathrm{PP},s}/p_{\mathrm{SI},s}$ is shown for the negative Q_f.

As a final remark, note that there are certain limitations on the values β can attain. For a negative Q_f, ψ_0 is less than 0 by definition and similarly, for a positive Q_f, ψ_0 is greater than 0. Then, one of the limits of β is

$$\beta_{\text{lim}} = \frac{W}{2}\sqrt{\frac{q^2 n_i}{2\epsilon_s kT}} e^{(-q\phi_{Fn})/2kT} \tag{B10}$$

for the case where $\psi_0 = 0$. Accordingly, the condition $\beta < \beta_{\text{lim}}$ should be satisfied for a negative Q_f and $\beta > \beta_{\text{lim}}$ should be satisfied for a positive Q_f. In addition, β should be greater than zero since the natural logarithm function in Eq. (B9) is undefined for negative inputs. Furthermore, the first and second terms of Eq. (B8) represent the charge density provided by holes and electrons, respectively. For small β, the first term of Eq. (B8) is dominant in determining Q_f, whereas for larger β the second term with the $\beta \tan \beta$ (where $y = W/2$) is the dominant one. However, these terms are not the inverse of each other, and the distribution of ψ is different, for example, for a positive Q_f on a p-type base (where $\beta > \beta_{\text{lim}}$) and a negative Q_f with similar magnitude on an n-type base (where $\beta < \beta_{\text{lim}}$). This problem can be bypassed by either varying the polarity of the ionized dopants to switch between accumulation and inversion conditions or by redefining the initial approximation in Eq. (B5) and, accordingly, the β in Eq. (B7), to be based on the carrier concentration that becomes dominant with larger Q_f.

[1] Felix Haase, Fabian Kiefer, Sören Schäfer, Christian Kruse, Jan Krügener, Rolf Brendel, and Robby Peibst, Interdigitated back contact solar cells with polycrystalline silicon on oxide passivating contacts for both polarities, Jpn. J. Appl. Phys. **56**, 08MB15 (2017).

[2] Evan Franklin, Kean Fong, Keith McIntosh, Andreas Fell, Andrew Blakers, Teng Kho, Daniel Walter, Da Wang, Ngwe Zin, Matthew Stocks, *et al.*, Design, fabrication and characterisation of a 24.4% efficient interdigitated back contact solar cell, Prog. Photovoltaics Res. Appl. **24**, 411 (2016).

[3] Simeon C. Baker-Finch and Keith R. McIntosh, Reflection of normally incident light from silicon solar cells with pyramidal texture, Prog. Photovoltaics Res. Appl. **19**, 406 (2011).

[4] Simeon C. Baker-Finch and Keith R. McIntosh, The contribution of planes, vertices, and edges to recombination at pyramidally textured surfaces, IEEE J. Photovoltaics **1**, 59 (2011).

[5] Yimao Wan and Keith R. Mcintosh, On the surface passivation of textured c-Si by PECVD silicon nitride, IEEE J. Photovoltaics **3**, 1229 (2013).

[6] Lachlan E. Black, Teng C. Kho, Keith R. Mcintosh, and Andres Cuevas, The influence of orientation and morphology on the passivation of crystalline silicon surfaces by Al_2O_3, Energy Procedia **55**, 750 (2014).

[7] Hang Cheong Sio, Teck Kong Chong, Sachin R. Surve, Klaus J. Weber, and Daniel H. Macdonald, Characterizing the influence of crystal orientation on surface recombination in silicon wafers, IEEE J. Photovoltaics **6**, 412 (2016).

[8] Martin Otto, Matthias Kroll, Thomas Käsebier, Roland Salzer, Andreas Tünnermann, and Ralf B. Wehrspohn, Extremely low surface recombination velocities in black silicon passivated by atomic layer deposition, Appl. Phys. Lett. **100**, 191603 (2012).10.1063/1.4714546

[9] Sören Schäfer, Catherin Gemmel, Sarah Kajari-Schröder, and Rolf Brendel, Light trapping and surface passivation of micron-scaled macroporous blind holes, IEEE J. Photovoltaics **6**, 397 (2016).

[10] Thomas Allen, James Bullock, Andres Cuevas, Simeon Baker-Finch, and Fouad Karouta, in *IEEE 40th Photovoltaic Specialist Conference* (IEEE, Denver, 2014), p. 562.

[11] G. Agostinelli, A. Delabie, P. Vitanov, Z. Alexieva, H. F. W. Dekkers, S. De Wolf, and G. Beaucarne, Very low surface recombination velocities on p-type silicon wafers passivated with a dielectric with fixed negative charge, Sol. Energy Mater. Sol. Cells **90**, 3438 (2006).

[12] Guillaume Von Gastrow, Ramon Alcubilla, Pablo Ortega, Marko Yli-Koski, Sonia Conesa-Boj, Anna Fontcuberta I. Morral, and Hele Savin, Analysis of the atomic layer deposited Al_2O_3 field-effect passivation in black silicon, Sol. Energy Mater. Sol. Cells **142**, 29 (2015).

[13] Paivikki Repo, Antti Haarahiltunen, Lauri Sainiemi, Marko Yli-Koski, Heli Talvitie, Martin C. Schubert, and Hele Savin, Effective passivation of black silicon surfaces by atomic layer deposition, IEEE J. Photovoltaics **3**, 90 (2013).

[14] Sören Schäfer, Deniz Turkay, Catherin Gemmel, Sarah Kajari-Schröder, and Rolf Brendel, in *Proceedings of the 31st European Photovoltaic Solar Energy Conference* (WIP, Hamburg, 2015), p. 457.

[15] Winfried Mönch, *Semiconductor Surfaces and Interfaces* (Springer, Berlin, Heidelberg, 2001), p. 24.

[16] D. J. Fitzgerald and A. S. Grove, Surface recombination in semiconductors, IEEE Trans. Electron Devices **15**, 426 (1968).

[17] Armin G. Aberle, Stefan W. Glunz, and Wilhelm Warta, Impact of illumination level and oxide parameters on Shockley-Read-Hall recombination at the Si-SiO_2 interface, J. Appl. Phys. **71**, 4422 (1992).

[18] W. Shockley and W. T. Read, Statistics of the recombination of holes and electrons, Phys. Rev. **87**, 835 (1952).

[19] R. N. Hall, Electron-hole recombination in germanium, Phys. Rev. **87**, 387 (1952).

[20] A. S. Grove and D. J. Fitzgerald, Surface effects on p-n junctions: Characteristics of surface space-charge regions under non-equilibrium conditions, Solid-State Electron. **9**, 783 (1966).

[21] Atlas user's manual, https://www.silvaco.com/.

[22] D. B. M. Klaassen, A unified mobility model for device simulation I. Model equations and concentration dependence, Solid-State Electron. **35**, 953 (1992).

[23] Andreas Schenk, Finite-temperature full random-phase approximation model of band gap narrowing for silicon device simulation, J. Appl. Phys. **84**, 1 (1998).

[24] Armin Richter, Stefan W. Glunz, Florian Werner, Jan Schmidt, and Andres Cuevas, Improved quantitative description of Auger recombination in crystalline silicon, Phys. Rev. B **86**, 165202 (2012).

[25] Pierre Saint-Cast, Youn Ho Heo, Etienne Billot, Peter Olwal, Marc Hofmann, Jochen Rentsch, Stefan W. Glunz, and Ralf Preu, Variation of the layer thickness to study the electrical property of PECVD Al_2O_3/c-Si interface, Energy Procedia **8**, 642 (2011).

[26] F. Werner, A. Cosceev, and J. Schmidt, Interface recombination parameters of atomic-layer-deposited Al_2O_3 on crystalline silicon, J. Appl. Phys. **111**, 073710 (2012).

[27] Lachlan E. Black and Keith R. Mcintosh, Modeling recombination at the Si-Al_2O_3 interface, IEEE J. Photovoltaics **3**, 936 (2013).

[28] Lachlan E. Black, Thomas Allen, Keith R. McIntosh, and Andres Cuevas, Effect of boron concentration on recombination at the p-Si-Al_2O_3 interface, J. Appl. Phys. **115**, 093707 (2014).

[29] Florian Werner, Atomic layer deposition of aluminum oxide on crystalline silicon: Fundamental interface properties and application to solar cells, Ph.D. thesis, Leibniz Universitat Hannover, (2013).

[30] Hans Lüth, *Solid Surfaces, Interfaces and Thin Films* (Springer International Publishing, Berlin, 2010), p. 330.

[31] John Gregory, Interaction of unequal double layers at constant charge, J. Colloid Interface Sci. **51**, 44 (1975).

[32] Ruy S. Bonilla, Frederick Woodcock, and Peter R. Wilshaw, Very low surface recombination velocity in n-type c-Si using extrinsic field effect passivation, J. Appl. Phys. **116**, 054102 (2014).

[33] K. J. Weber and H. Jin, Improved silicon surface passivation achieved by negatively charged silicon nitride films, Appl. Phys. Lett. **94**, 063509 (2009).

[34] Florian Werner and Jan Schmidt, Manipulating the negative fixed charge density at the c-Si/Al_2O_3 interface, Appl. Phys. Lett. **104**, 091604 (2014).

[35] Vivek Sharma, Clarence Tracy, Dieter Schroder, Stanislau Herasimenka, William Dauksher, and Stuart Bowden, Manipulation of K center charge states in silicon nitride films to achieve excellent surface passivation for silicon solar cells, Appl. Phys. Lett. **104**, 053503 (2014).

[36] Ruy S. Bonilla, Christian Reichel, Martin Hermle, and Peter R. Wilshaw, in *Gettering and Defect Engineering in Semiconductor Technology XV*, Solid State Phenomena, Vol. 205 (Trans Tech Publ, Oxford, 2014), p. 346.

[37] Ruy S. Bonilla, Christian Reichel, Martin Hermle, Phillip Hamer, and Peter R. Wilshaw, Long term stability of c-Si surface passivation using corona charged SiO_2, Appl. Surf. Sci. **412**, 657 (2017).

[38] Ruy S. Bonilla and Peter R. Wilshaw, Potassium ions in SiO_2: Electrets for silicon surface passivation, J. Phys. D: Appl. Phys. **51**, 025101 (2017).

[39] Katherine A. Collett, Siyao Du, Gabrielle Bourret-Sicotte, Zhaohua Luo, Phillip Hamer, Brett Hallam, Ruy S. Bonilla, and Peter R. Wilshaw, Scalable techniques for producing field-effect passivation in high-efficiency silicon solar cells, IEEE J. Photovoltaics **9**, 26 (2019).

[40] Bruce E. Deal, Maija Sklar, Andrew S. Grove, and Edward H. Snow, Characteristics of the surface-state charge (Q_{ss}) of thermally oxidized silicon, J. Electrochem. Soc. **114**, 266 (1967).

[41] H. P. Vyas, G. D. Kirchner, and S. J. Lee, Fixed charge density (Q_{ss}) at the Si-SiO_2 interface for thin oxides, J. Electrochem. Soc. **129**, 1757 (1982).

[42] A. G. Aberle, S. W. Glunz, A. W. Stephens, and M. A. Green, High-eficiency silicon solar cells: Si/SiO_2, interface parameters and their impact on device performance, Prog. Photovoltaics Res. Appl. **2**, 265 (1994).

[43] S. W. Glunz, D. Biro, S. Rein, and W. Warta, Field-effect passivation of the SiO_2-Si interface, J. Appl. Phys. **86**, 683 (1999).

[44] G. Dingemans, M. C. M. Van De Sanden, and W. M. M. Kessels, Excellent si surface passivation by low temperature SiO_2 using an ultrathin Al_2O_3 capping film, Phys. Status Solidi RRL–Rapid Res. Lett. **5**, 22 (2011).

[45] G. Dingemans, N. M. Terlinden, M. A. Verheijen, M. C. M. Van de Sanden, and W. M. M. Kessels, Controlling the fixed charge and passivation properties of Si(100)/Al_2O_3 interfaces using ultrathin SiO_2 interlayers synthesized by atomic layer deposition, J. Appl. Phys. **110**, 093715 (2011).

[46] Daniel K. Simon, Paul M. Jordan, Thomas Mikolajick, and Ingo Dirnstorfer, On the control of the fixed charge densities in Al_2O_3-based silicon surface passivation schemes, ACS Appl. Mater. Interfaces **7**, 28215 (2015).

[47] R. Hezel and K. Jaeger, Low-temperature surface passivation of silicon for solar cells, J. Electrochem. Soc. **136**, 518 (1989).

[48] Stefan Dauwe, Jan Schmidt, Axel Metz, and Rudolf Hezel, in *Conference Record of the Twenty-Ninth IEEE Photovoltaic Specialists Conference, 2002* (IEEE, New Orleans, 2002), p. 162.

[49] Yimao Wan, Keith R. McIntosh, Andrew F. Thomson, and Andres Cuevas, in *2012 IEEE 38th Photovoltaic Specialists Conference (PVSC) PART 2* (IEEE, Austin, 2012), p. 1.

[50] Machteld W. P. E. Lamers, Keith T. Butler, John H. Harding, and Arthur Weeber, Interface properties of a-SiN_x:H/Si to improve surface passivation, Sol. Energy Mater. Sol. Cells **106**, 17 (2012).

[51] Bram Hoex, J. J. H. Gielis, M. C. M. Van de Sanden, and W. M. M. Kessels, On the c-Si surface passivation mechanism by the negative-charge-dielectric Al_2O_3, J. Appl. Phys. **104**, 113703 (2008).

[52] Gijs Dingemans and W. M. M. Kessels, Status and prospects of Al_2O_3-based surface passivation schemes for silicon solar cells, J. Vac. Sci. Technol. A: Vac., Surf., Films **30**, 040802 (2012).

[53] Friederike Kersten, Alexander Schmid, Stefan Bordihn, Jörg W. Müller, and Johannes Heitmann, Role of annealing conditions on surface passivation properties of ALD Al_2O_3 films, Energy Procedia **38**, 843 (2013).

[54] Lachlan E. Black, Thomas Allen, Andres Cuevas, Keith R. McIntosh, Boris Veith, and Jan Schmidt, Thermal stability of silicon surface passivation by APCVD Al_2O_3, Sol. Energy Mater. Sol. Cells **120**, 339 (2014).

[55] Stefaan De Wolf, Sara Olibet, and Christophe Ballif, Stretched-exponential a-Si:H/c-Si interface recombination decay, Appl. Phys. Lett. **93**, 032101 (2008).

[56] Sara Olibet, Evelyne Vallat-Sauvain, and Christophe Ballif, Model for a-Si:H/c-Si interface recombination based on the amphoteric nature of silicon dangling bonds, Phys. Rev. B **76**, 035326 (2007).

[57] Sara Olibet, Evelyne Vallat-Sauvain, Luc Fesquet, Christian Monachon, Aïcha Hessler-Wyser, Jérôme Damon-Lacoste, Stefaan De Wolf, and Christophe Ballif, Properties of interfaces in amorphous/crystalline silicon heterojunctions, Phys. Status Solidi (a) **207**, 651 (2010).

[58] Caspar Leendertz, N. Mingirulli, T. F. Schulze, Jean-Paul Kleider, Bernd Rech, and Lars Korte, Discerning passivation mechanisms at a-Si:H/c-Si interfaces by means of photoconductance measurements, Appl. Phys. Lett. **98**, 202108 (2011).

[59] Raghavasimhan Sreenivasan, Paul C. McIntyre, Hyoungsub Kim, and Krishna C. Saraswat, Effect of impurities on the fixed charge of nanoscale HfO_2 films grown by atomic layer deposition, Appl. Phys. Lett. **89**, 112903 (2006).

[60] Yan-Kai Chiou, Che-Hao Chang, and Tai-Bor Wu, Characteristics of hafnium oxide grown on silicon by atomic-layer deposition using tetrakis (ethylmethylamino) hafnium and water vapor as precursors, J. Mater. Res. **22**, 1899 (2007).

[61] Jun Wang, Seyyed Sadegh Mottaghian, and Mahdi Farrokh Baroughi, Passivation properties of atomic-layer-deposited hafnium and aluminum oxides on Si surfaces, IEEE Trans. Electron. Devices **59**, 342 (2012).

[62] Jhuma Gope, Vandana, Neha Batra, Jagannath Panigrahi, Rajbir Singh, K. K. Maurya, Ritu Srivastava, and P. K. Singh, Silicon surface passivation using thin HfO_2 films by atomic layer deposition, Appl. Surf. Sci. **357**, 635 (2015).

[63] Jie Cui, Yimao Wan, Yanfeng Cui, Yifeng Chen, Pierre Verlinden, and Andres Cuevas, Highly effective electronic passivation of silicon surfaces by atomic layer deposited hafnium oxide, Appl. Phys. Lett. **110**, 021602 (2017).

[64] Xuemei Cheng, Päivikki Repo, Haug Halvard, Alexander Pyymaki Perros, Erik Stensrud Marstein, Marisa Di Sabatino, and Hele Savin, Surface passivation properties of HfO_2 thin film on n-type crystalline Si, IEEE J. Photovoltaics **7**, 479 (2017).

[65] Yi Ma, T. Yasuda, and G. Lucovsky, Fixed and trapped charges at oxide-nitride-oxide heterostructure interfaces formed by remote plasma enhanced chemical vapor deposition, J. Vac. Sci. Technol. B: Microelectron. Nanometer Struct. Process., Meas., Phenom. **11**, 1533 (1993).

[66] Ruy S. Bonilla, Christian Reichel, Martin Hermle, and Peter R. Wilshaw, On the location and stability of charge in SiO_2/SiN_x dielectric double layers used for silicon surface passivation, J. Appl. Phys. **115**, 144105 (2014).

[67] Zhong Lu, Zi Ouyang, Nicholas Grant, Yimao Wan, Di Yan, and Alison Lennon, Manipulation of stored charge in anodic aluminium oxide/SiO_2 dielectric stacks by the use of pulsed anodisation, Appl. Surf. Sci. **363**, 296 (2016).

[68] Sebastian Mack, Andreas Wolf, Christoph Brosinsky, Simon Schmeisser, Achim Kimmerle, Pierre Saint-Cast, Marc Hofmann, and Daniel Biro, Silicon surface passivation by thin thermal oxide/PECVD layer stack systems, IEEE J. Photovoltaics **1**, 135 (2011).

[69] Shubham Duttagupta, Fa-Jun Ma, Bram Hoex, and Armin G. Aberle, in *2013 IEEE 39th Photovoltaic Specialists Conference (PVSC)* (IEEE, Tampa, 2013), p. 1776.

[70] Shubham Duttagupta, Ziv Hameiri, Thomas Grosse, Dirk Landgraf, Bram Hoex, and Armin G. Aberle, Dielectric charge tailoring in PECVD SiO_x/SiN_x stacks and application at the rear of Al local back surface field Si wafer solar cells, IEEE J. Photovoltaics **5**, 1014 (2015).

[71] N. M. Terlinden, G. Dingemans, V. Vandalon, R. H. E. C. Bosch, and W. M. M. Kessels, Influence of the SiO_2 interlayer thickness on the density and polarity of charges in $Si/SiO_2/Al_2O_3$ stacks as studied by optical second-harmonic generation, J. Appl. Phys. **115**, 033708 (2014).

[72] B. W. H. van de Loo, H. C. M. Knoops, G. Dingemans, G. J. M. Janssen, M. W. P. E. Lamers, I. G. Romijn, A. W. Weeber, and W. M. M. Kessels, Zero-charge SiO_2/Al_2O_3 stacks for the simultaneous passivation of $n+$ and $p+$ doped silicon surfaces by atomic layer deposition, Sol. Energy Mater. Sol. Cells **143**, 450 (2015).

[73] Armin Richter, Jan Benick, Martin Hermle, and Stefan W. Glunz, Excellent silicon surface passivation with 5 Å thin ALD Al_2O_3 layers: Influence of different thermal post-deposition treatments, Phys. Status Solidi RRL–Rapid Res. Lett. **5**, 202 (2011).

[74] D. Schuldis, A. Richter, J. Benick, P. Saint-Cast, M. Hermle, and S. W. Glunz, Properties of the c-Si/Al_2O_3 interface of ultrathin atomic layer deposited Al_2O_3 layers capped by SiN_x for c-Si surface passivation, Appl. Phys. Lett. **105**, 231601 (2014).

[75] Daniel K. Simon, Paul M. Jordan, Ingo Dirnstorfer, Frank Benner, Claudia Richter, and Thomas Mikolajick, Symmetrical Al_2O_3-based passivation layers for p and n-type silicon, Sol. Energy Mater. Sol. Cells **131**, 72 (2014).

[76] Simeon C. Baker-Finch, and Keith R. McIntosh, in *Proceedings of the 46th ANZSES Conference* (ANZSES, Melbourne, 2008), Vol. 304.

[77] Andre Stesmans and V. V. Afanasev, Invasive nature of corona charging on thermal Si/SiO_2 structures with nanometer-thick oxides revealed by electron spin resonance, Appl. Phys. Lett. **82**, 2835 (2003).

[78] Hao Jin, K. J. Weber, N. C. Dang, and W. E. Jellett, Defect generation at the Si-SiO_2 interface following corona charging, Appl. Phys. Lett. **90**, 262109 (2007).

[79] D. K. Schroder, M. S. Fung, R. L. Verkuil, S. Pandey, W. H. Howland, and M. Kleefstra, Corona-oxide-semiconductor device characterization, Solid-State Electron. **42**, 505 (1998).

[80] Marshall Wilson, Jacek Lagowski, Lubek Jastrzebski, Alexandre Savtchouk, and Vladimir Faifer, in *AIP Conference Proceedings* (AIP, Gaithersburg, 2001), Vol. 550, p. 220.

[81] Teng C. Kho, Simeon C. Baker-Finch, and Keith R. McIntosh, The study of thermal silicon dioxide electrets formed by corona discharge and rapid-thermal annealing, J. Appl. Phys. **109**, 053108 (2011).

[82] Keith R. McIntosh and Luke P. Johnson, Recombination at textured silicon surfaces passivated with silicon dioxide, J. Appl. Phys. **105**, 124520 (2009).

[83] Keith R. McIntosh and Lachlan E. Black, On effective surface recombination parameters, J. Appl. Phys. **116**, 014503 (2014).

[84] E. Yablonovitch, D. L. Allara, C. C. Chang, T. Gmitter, and T. B. Bright, Unusually low Surface-recombination Velocity on Silicon and Germanium Surfaces, Phys. Rev. Lett. **57**, 249 (1986).

[85] Reinhard B. M. Girisch, Robert P. Mertens, and Roger F. De Keerscmaecker, Determination of Si-SiO$_2$ interface recombination parameters using a gate-controlled point-junction diode under illumination, IEEE Trans. Electron Devices **35**, 203 (1988).

[86] Yuan Taur, An analytical solution to a double-gate MOSFET, IEEE Electron Device Lett. **21**, 245 (2000).

[87] Xiaoshi Jin, Xi Liu, Jung-Hee Lee, and Jong-Ho Lee, A continuous current model of fully-depleted symmetric double-gate MOSFETs considering a wide range of body doping concentrations, Semicond. Sci. Technol. **25**, 055018 (2010).

[88] Xiaoshi Jin, Xi Liu, Meile Wu, Rongyan Chuai, Jung Hee Lee, and Jong Ho Lee, A unified analytical continuous current model applicable to accumulation mode (junctionless) and inversion mode MOSFETs with symmetric and asymmetric double-gate structures, Solid-State Electron. **79**, 206 (2013).